JOURNAL OF COMPUTATIONAL PHYSICS **143,** 49–69 (1998)
ARTICLE NO. CP985972

Application of Adaptive Quadrature to Axi-symmetric Vortex Sheet Motion

Qing Nie* and Greg Baker†

Institute for Mathematics and Its Applications, 514 Vincent Hall, 206 Church Street S.E., Minneapolis, Minnesota 55455-0436; and † Department of Mathematics, Ohio State University, Columbus, Ohio 43210-1174
E-mail: * nie@ima.umn.edu and † baker@math.ohio-state.edu

Received June 2, 1997; revised December 24, 1997

Studies of the formation of fine structures on free surfaces in liquids, such as curvature singularities or interface pinching, demand that the motion of the interface must be computed very accurately. Boundary integral techniques are a popular choice in such studies because they reduce the dimension of the problem by one. On the other hand, the boundary integrals are singular, and their accurate evaluation can prove quite challenging. In two-dimensional motion, the interface is just a curve. When this curve is closed or periodic, the singularity in the integrand may be removed and the trapezoidal rule may be applied with spectral accuracy. Unfortunately, the nature of the singularity in the integrand for three-dimensional motion is much more difficult to treat. In this paper, we present an accurate adaptive quadrature to compute the motion of a vortex sheet in axi-symmetric flow. The technique is based on a vector-potential formulation which offers some computational advantages over other methods based on the Biot–Savart integral. Direct numerical computations show that our technique is much more accurate and efficient than existing techniques. We apply our technique to study the evolution of an initially spherical vortex sheet. We present evidence of the formation of a 3/2 power singularity in the curvature of the vortex sheet.

Key Words: axi-symmetric vortex sheets; adaptive integration.

1. INTRODUCTION

Boundary integral techniques provide a popular approach to studying free-surface motion in liquids, covering a wide range of phenomena. Some examples are the propagation of waves in inviscid liquids [1] and the motion of drops in very viscous liquids [2]. One of the major features of boundary integral techniques is that they provide an evolution equation for the motion of the interface explicitly. Since there is no need to determine the flow field away from the interface, the dimension of the problem is reduced by one. On the other hand, the boundary integrals are principal-value integrals and their accurate evaluation can be very challenging. This is particularly true in studies of the formation of fine structures on the interface, such as curvature singularities or interface pinching.

In two-dimensional motion there have been several successful studies of interfacial motion. In particular, spectrally accurate methods are available when the interface is closed (as in rising bubbles [3]) or is periodic in open geometry (as in water waves [1] or Rayleigh–Taylor instability [4]). First, the pole singularity in the principal-value integral may be removed by the subtraction of a simple integral, and then the trapezoidal rule may be applied with spectral accuracy to the resulting periodic integral [5, 6]. The high order of accuracy proves very desirable in studies of fine features, such as the formation of a curvature singularity in vortex sheet motion [7] or during the Rayleigh–Taylor instability [8].

The situation is very different for the computation of axi-symmetric flows. The principal-value integrals involve complete elliptic integrals which contain logarithmic singularities. The singularity in the integrand can be weakened, but cannot be removed completely as in the two-dimensional case: some derivative of the integrand will remain singular. Further, the integrand shows strong variations especially near the poles [9], which makes the design of an accurate quadrature difficult. For example, a vortex ring method [10] with a correction term to treat the principal value also finds difficulties at the pole: the order of the method is reduced to $O(h)$ near the poles where h is the spacing between the rings. An improvement to this method has been found recently [11] by an ingenious analytic approximation to the integrand near the poles. The improved method is still only $O(h^3 \log h)$. A different approach [9, 12] is to insert more quadrature points through interpolation when performing the integration at collocation points near the poles, but numerical instabilities appear in the vortex sheet near the poles after a short time. This behavior illustrates a useful principle in designing methods for vortex sheet motion: not only must the numerical errors from the boundary integrals be small, but they should also be relatively smooth to avoid the onset of instabilities.

There have been attempts [13, 14] to study the formation of curvature singularities in axi-symmetric vortex sheets. The numerical calculations were based on the vortex ring method [10], and while evidence for the existence of the singularity was found, not enough resolution was possible to identify the nature of the singularity. As we will show, it is necessary to compute the boundary integral to an accuracy of about 10^{-20} to determine the precise form of the singularity. This requirement is probably too severe even for methods of moderate order. In this paper, we present efficient and accurate integration for axi-symmetric vortex sheet computations based on high order adaptive Gauss–Kronrod and Clenshaw–Curtis quadratures.

The conventional approach to stating a boundary integral method for vortex sheet motion is in terms of the vorticity distribution along the sheet [15]. We introduce a different representation based on a dipole distribution, because it is easier to weaken the singularity in the principal-value integrals by the subtraction of a suitable analytic expression. In our first series of tests, we show that singularity reduction in the integrands of the dipole distribution provides a better formulation for the accurate numerical evaluation of the velocity of the vortex sheet. We calculate the flow around a spherical vortex sheet held fixed in time by three different methods. In Method A, we apply the six-point Gaussian quadrature to the Biot–Savart integral. In Method B, we follow previous work [10] by using a point vortex method with the axi-symmetric Van der Vooren correction. Although the numerical integration is of lower order, the explicit treatment of the singularity in the integrands in Method B leads to better accuracy. In Method C, we apply the six-point Gaussian quadrature to the dipole representation after singularity reduction. This method proves the best of the three. All three methods suffer from loss of accuracy near the poles.

To control accuracy, we apply adaptive numerical integration to the integrals of the dipole distribution after singularity reduction. In one approach, we use Gauss–Kronrod quadrature directly on the integrals in the standard adaptive way. In the other approach, we note that the presence of the logarithmic singularity in the complete elliptic functions can be treated by a specialized adaptive quadrature. We first approximate the two complete elliptic integrals in the integrands by the sum of two parts, a regular part and a logarithmic part; then we apply Gauss–Kronrod quadrature adaptively to the regular part and the modified Clenshaw–Curtis quadrature adaptively to the logarithmic part. Our tests indicate that both adaptive approaches are significantly better than the non-adaptive approaches. The adaptive Clenshaw–Curtis method is the more efficient.

We apply the adaptive Clenshaw–Curtis method to the evolution of an initially spherical vortex sheet up to the time just before the formation of a curvature singularity. We find no evidence of numerical instabilities. Next, we follow the standard approach to detecting curvature singularities in vortex sheets by fitting the Fourier spectrum to a form indicative of the presence of a singularity with an algebraic power. We find that it is necessary to have an accuracy of about 10^{-20} to determine the power of the singularity as $3/2$.

The organization of the paper is as follows. In Section 2, we derive the equations of motion for a full three-dimensional vortex sheet and its axi-symmetric version. We give both formulations, the one based on the Biot–Savart law, and the other based on the dipole distribution. We describe the numerical techniques in Section 3, and discuss and compare the performance of the different methods in Section 4. Finally, we present the results of the calculation of the motion of an axi-symmetric sheet using the adaptive Clenshaw–Curtis quadrature.

2. FORMULATIONS

In this section, we give the boundary integral equations for a three-dimensional vortex sheet; then we obtain the special form for an axi-symmetric sheet. We follow the same notation as in [15], but we derive the equations from a different point of view based on representing the vortex sheet by a dipole distribution. Dipole distributions have already been used to study the evolution of an interface between a liquid and gas [9], but there are some minor differences when the interface is a vortex sheet in a homogeneous liquid.

Let S denote a closed vortex sheet, which divides the fluid region into two parts: an outside region D_+ and an inside region D_-. The velocity and pressure fields are $(u_\pm, p_\pm)$, respectively. The Euler equations of motion are

$$\frac{\partial \mathbf{u}_\pm}{\partial t} + \mathbf{u}_\pm \cdot \nabla \mathbf{u}_\pm + \nabla p_\pm = 0 \qquad \text{in } D_\pm, \tag{1}$$

$$\nabla \cdot \mathbf{u}_\pm = 0 \qquad \text{in } D_\pm, \tag{2}$$

$$\nabla \times \mathbf{u}_\pm = 0 \qquad \text{in } D_\pm/S. \tag{3}$$

Kinematic and dynamic considerations require the following conditions on the vortex sheet,

$$\mathbf{n} \cdot \mathbf{u}_+ = \mathbf{n} \cdot \mathbf{u}_- \text{ and } p_+ = p_- \qquad \text{on } S, \tag{4}$$

where **n** is the normal to S pointing into D_+. It is the jump in tangential components of the velocity that characterizes the vortex sheet.

We introduce two surface coordinates α and β and express the location of the interface as $\mathbf{X}(\alpha, \beta, t)$. These coordinates will be defined by the requirement that the motion of the sheet is "Lagrangian." By that we mean a "particle" on S labeled by α and β moves with the velocity

$$\frac{\partial \mathbf{X}}{\partial t} = \mathbf{u} \equiv \frac{1}{2}(\mathbf{u}_+ + \mathbf{u}_-) \qquad \text{on } S. \tag{5}$$

Note that the normal component of the velocity of the sheet matches that of the two liquids as required by (4).

Due to (2), (3), there exist potential functions $\phi_\pm$ such that

$$\mathbf{u}_\pm = \nabla \phi_\pm \qquad \text{in } D_\pm / S. \tag{6}$$

We introduce a dipole distribution $\mu(\alpha, \beta, t)$ on the sheet. According to potential theory [16, 17], a dipole distribution generates a potential function

$$w(\mathbf{x}) = -\frac{1}{4\pi} \int_S \mu(\mathbf{x}')\mathbf{n}(\mathbf{x}') \cdot \nabla_{\mathbf{x}'} \left(\frac{1}{|\mathbf{x} - \mathbf{x}'|} \right) d\mathbf{x}' \qquad \text{in } D_\pm \tag{7}$$

with the properties

$$w(\mathbf{x}) = \begin{cases} \phi_+ & \mathbf{x} \text{ in } D_+ \\ \phi_- & \mathbf{x} \text{ in } D_- \end{cases} \tag{8}$$

and $\mu = \phi_+ - \phi_-$ on S. The potential ϕ_+ vanishes at infinity, which means there is no far field flow. If a far field flow is present, it must be added separately. In our study, we assume there is no far field flow.

Define

$$\phi = \frac{1}{2}(\phi_+ + \phi_-) \qquad \text{on } S. \tag{9}$$

Then from potential theory, we have

$$\phi(\mathbf{x}) = -\frac{1}{4\pi} -\!\!\!\!\!\!\int_S \mu(\mathbf{x}')\mathbf{n}(\mathbf{x}') \cdot \nabla_{\mathbf{x}'} \left(\frac{1}{|\mathbf{x} - \mathbf{x}'|} \right) d\mathbf{x}' \qquad \text{on } S. \tag{10}$$

As a consequence, the motion of the sheet is given by

$$\mathbf{X}_t(\alpha, \beta, t) = \nabla \phi. \tag{11}$$

The evolution equation for μ is obtained as follows. First we determine the rate of change of the potential along the trajectory of a surface particle moving according to (5). By differentiating $\phi_\pm(\alpha, \beta, t) = \phi_\pm(\mathbf{X}(\alpha, \beta, t), t)$ with respect to time, keeping the surface coordinates α and β fixed, we obtain

$$\frac{\partial \phi_\pm}{\partial t} = \left. \frac{\partial \phi_\pm}{\partial t} \right|_{\mathbf{x}} + \mathbf{u} \cdot \nabla \phi_\pm. \tag{12}$$

The rate of change of the potential at a fixed point in space can be obtained by integrating (1),

$$\left.\frac{\partial \phi}{\partial t}\right|_{\mathbf{x}} = -\frac{1}{2}\mathbf{u}\cdot\mathbf{u} - p + c, \tag{13}$$

where c is a constant. Upon substituting the result into (12), we obtain

$$\frac{\partial \phi_\pm}{\partial t} = \left(\mathbf{u} - \frac{1}{2}\mathbf{u}_\pm\right)\cdot\mathbf{u}_\pm - p_\pm + c_\pm. \tag{14}$$

By subtracting the rate of change of the potential on either side of the sheet, we find

$$\frac{\partial \mu}{\partial t} = \left(\mathbf{u} - \frac{1}{2}\mathbf{u}_+\right)\cdot\mathbf{u}_+ - \left(\mathbf{u} - \frac{1}{2}\mathbf{u}_-\right)\cdot\mathbf{u}_- + c_+ - c_-. \tag{15}$$

The value of the definition of the velocity for the vortex sheet (5) now becomes clear since (15) simplifies to

$$\mu = \mu|_{t=0} + (c_+ - c_-)t \qquad \text{on } S. \tag{16}$$

Since a dipole that is constant on S induces only constant potentials inside and outside, the contribution $(c_+ - c_-)t$ has no dynamical significance, and we may assume $c_+ = c_- = 0$ without loss of generality. In other words, we may consider $\mu = \mu(\alpha, \beta)$ on S to be independent of time and given by the initial conditions.

Next, we describe how $\mathbf{u}$ is calculated. We assume that our coordinate system has the property that $\mathbf{X}_\beta$, $\mathbf{X}_\alpha$, and $\mathbf{n}$ form a right-hand system with

$$\mathbf{n} = \frac{\mathbf{X}_\beta \times \mathbf{X}_\alpha}{|\mathbf{X}_\beta \times \mathbf{X}_\alpha|}. \tag{17}$$

The Greek subscripts refer to differentiation with respect to the surface coordinates. We take the gradient of w as given by (7) and "integrate by parts" over the vortex sheet. Then we take the average of the limiting values on either side of the sheet to obtain

$$\mathbf{u} = -\frac{1}{4\pi}\,⨍_S \left(\mu'_\beta \mathbf{X}'_\alpha - \mu'_\alpha \mathbf{X}'_\beta\right) \times \left(\frac{\mathbf{X} - \mathbf{X}'}{|\mathbf{X} - \mathbf{X}'|^3}\right) d\alpha'\, d\beta'. \tag{18}$$

We have introduced the notation $\mu' = \mu(\alpha', \beta')$, etc., for convenience. This equation is the same as that obtained from the Biot–Savart law [15].

We obtain a different expression for $\mathbf{u}$ by differentiating ϕ (see (11)). In particular,

$$\mathbf{u} = \frac{\partial \phi}{\partial n}\mathbf{n} + \phi_\alpha \frac{\mathbf{n} \times \mathbf{X}_\beta}{|\mathbf{X}_\alpha \times \mathbf{X}_\beta|} + \phi_\beta \frac{\mathbf{X}_\alpha \times \mathbf{n}}{|\mathbf{X}_\alpha \times \mathbf{X}_\beta|}. \tag{19}$$

The simplest way to determine $\partial\phi/\partial\mathbf{n}$ is through the associated vector potential $\mathbf{A}$, which has the following integral representation [17],

$$\mathbf{A}(\mathbf{x}) = \frac{1}{4\pi}\,⨍_S \mu(\mathbf{x}')\mathbf{n}(\mathbf{x}') \times \nabla_{\mathbf{x}'}\left(\frac{1}{|\mathbf{x} - \mathbf{x}'|}\right) d\mathbf{x}' \qquad \text{on } S. \tag{20}$$

Specifically,

$$\begin{aligned}\frac{\partial\phi}{\partial n} &= \mathbf{n}\cdot(\nabla\times\mathbf{A})\\ &= [(\mathbf{A}\cdot\mathbf{X}_\alpha)_\beta - (\mathbf{A}\cdot\mathbf{X}_\beta)_\alpha]\frac{1}{|\mathbf{X}_\alpha\times\mathbf{X}_\beta|}.\end{aligned}\tag{21}$$

Notice that once ϕ and **A** have been computed through (10) and (20), we differentiate them with respect to the surface coordinates to obtain the velocity components in (19). This then provides an alternate approach to computing the motion of the vortex sheet.

The advantage of using the surface integrals (10) and (19) is that the identities

$$-\frac{1}{4\pi}\oint \mathbf{n}(\mathbf{x}')\cdot\nabla_{\mathbf{x}'}\left(\frac{1}{|\mathbf{x}-\mathbf{x}'|}\right)d\mathbf{x}' = \frac{1}{2},\tag{22}$$

$$\frac{1}{4\pi}\oint \mathbf{n}(\mathbf{x}')\times\nabla_{\mathbf{x}'}\left(\frac{1}{|\mathbf{x}-\mathbf{x}'|}\right)d\mathbf{x}' = 0\tag{23}$$

may be used to reduce the singularities in their integrands [9]. For example, **A** can be rewritten as

$$\mathbf{A}(\mathbf{x}) = \frac{1}{4\pi}\oint(\mu(\mathbf{x}')-\mu(\mathbf{x}))\mathbf{n}(\mathbf{x}')\times\nabla_{\mathbf{x}'}\left(\frac{1}{|\mathbf{x}-\mathbf{x}'|}\right)d\mathbf{x}' \qquad \text{on } S.\tag{24}$$

We will show specifically in the case of axi-symmetric flow how the singularities in the integrands have been reduced.

For an axi-symmetric vortex sheet, we may represent the sheet location as

$$\mathbf{X} = r(\alpha,t)\mathbf{e}_r + z(\alpha,t)\mathbf{e}_z\tag{25}$$

using the cylindrical coordinates (r, z). The motion of the sheet is assumed independent of the azimuthal angle $\beta=\theta$. As noted before [15] for motion without swirl, the Biot–Savart integral (18) becomes

$$r_t = \frac{1}{4\pi r}\oint \mu'_\alpha(z'-z)B_0(\alpha,\alpha')[F(k)+B_1(\alpha,\alpha')E(k)]\,d\alpha',\tag{26}$$

$$z_t = \frac{1}{4\pi}\oint \mu'_\alpha B_0(\alpha,\alpha')[F(k)+B_2(\alpha,\alpha')E(k)]\,d\alpha',\tag{27}$$

where $F(k)$ and $E(k)$ are the complete elliptic integrals

$$F(k) = \int_0^{\pi/2}(1-k^2\cos^2(\beta))^{-1/2}\,d\beta, \qquad E(k) = \int_0^{\pi/2}(1-k^2\cos^2(\beta))^{1/2}\,d\beta\tag{28}$$

of the first and second kind respectively, with

$$k^2 = \frac{4rr'}{(z-z')^2+(r+r')^2}.\tag{29}$$

The other quantities are

$$B_0(\alpha,\alpha') = \frac{2}{((z-z')^2+(r+r')^2)^{1/2}},\tag{30}$$

$$B_1(\alpha,\alpha') = -\frac{(z'-z)^2 + r'^2 + r^2}{(z-z')^2 + (r-r')^2}, \tag{31}$$

$$B_2(\alpha,\alpha') = \frac{r'^2 - r^2 - (z'-z)^2}{(z-z')^2 + (r-r')^2}. \tag{32}$$

Now our notation reflects the dependency on only one surface coordinate, $r' = r(\alpha')$, etc.

In the alternate formulation, (19) becomes

$$r_t = \left(\phi_\alpha r_\alpha - \frac{\psi_\alpha}{r} z_\alpha\right)\frac{1}{s_\alpha^2}, \tag{33}$$

$$z_t = \left(\phi_\alpha z_\alpha + \frac{\psi_\alpha}{r} r_\alpha\right)\frac{1}{s_\alpha^2}, \tag{34}$$

where $s_\alpha^2 = r_\alpha^2 + z_\alpha^2$ and $\psi = r\mathbf{A}\cdot\mathbf{e}_\theta$ is a pseudo-streamfunction. Note that $\mathbf{A}$ has only one non-vanishing component. By using (22), (23), we may express the potential function (10) as

$$\phi = \frac{1}{4\pi} \mathrm{P}\!\!\!\int (\mu' - \mu) B_0(\alpha,\alpha')[z'_\alpha F(k) + C_1(\alpha,\alpha') E(k)]\, d\alpha' + \frac{1}{2}\mu, \tag{35}$$

and the pseudo-streamfunction (obtained from (20)) as

$$\psi = \frac{1}{4\pi} \mathrm{P}\!\!\!\int (\mu' - \mu) B_0(\alpha,\alpha')\{[r'_\alpha r' - z'_\alpha (z - z')]F(k) + C_2(\alpha,\alpha') E(k)\}\, d\alpha', \tag{36}$$

where

$$C_1 = -\frac{(z-z')[z'_\alpha (z-z') - 2r' r'_\alpha] + (r^2 - r'^2) z'_\alpha}{(z-z')^2 + (r-r')^2} \tag{37}$$

$$C_2 = \frac{(z-z')([z'_\alpha (z-z') - r'_\alpha r'](z-z') + z'_\alpha (r^2 + r'^2)) + (r^2 - r'^2) r'_\alpha r'}{(z-z')^2 + (r-r')^2}. \tag{38}$$

In order to design good numerical methods for the integrals, we must understand the nature of the singularities in the integrands. First, we consider the asymptotic behavior of the integrands in (26), (27) when the integration variable α' is close to the field point at α. For $r \equiv r(\alpha) \neq 0$, the leading order terms of the integrands are

$$-\frac{2r\mu_\alpha z_\alpha}{s_\alpha^2(\alpha' - \alpha)} \qquad \text{and} \qquad \frac{2\mu_\alpha r_\alpha}{s_\alpha^2(\alpha' - \alpha)}, \tag{39}$$

respectively. Clearly, the integrands have pole singularities $1/(\alpha' - \alpha)$ except right on the axis.

In the other formulation, the integrands in (35), (36) exhibit the following asymptotic behavior,

$$-\frac{z_\alpha \mu_\alpha}{r}(\alpha' - \alpha)\ln|\alpha - \alpha'| \qquad \text{and} \qquad -2\mu_\alpha r, \tag{40}$$

respectively. Therefore, these integrands are continuous even though they have discontinuous derivatives. This information will prove very valuable in the design of effective numerical methods.

3. NUMERICAL METHODS

We describe the numerical methods to evaluate the velocity of the vortex sheet in three parts: evaluation of the complete elliptic integrals of the first and second kind; adaptive numerical quadratures; and their specific application to the vortex sheet.

3.1. *Evaluation of the Elliptic Integrals*

In [18, p. 297], there are recursive formulae for the evaluation of both $F(k)$ and $E(k)$,

$$F = \frac{\pi}{2}(1 + G_1)(1 + G_2)(1 + G_3)\cdots, \qquad E = F\left(1 - \frac{k^2}{2}H\right), \tag{41}$$

where

$$H = 1 + \frac{G_1}{2}\left(1 + \frac{G_2}{2}\left(1 + \frac{G_3}{2}(\cdots)\cdots\right)\cdots\right), \tag{42}$$

and G_i is given by the recursion

$$G_0 = k, \qquad G_i = \frac{1 - \sqrt{1 - G_{i-1}^2}}{1 + \sqrt{1 - G_{i-1}^2}}. \tag{43}$$

This method is very robust computationally. However, the number of iterations for a given tolerance depends on k. In general, more iterations are needed when k is close to 1.

The other widely used technique for the computation of E and F is a polynomial approximation. From [18, p. 297] and [19, p. 170], we know

$$F = \ln(4) + \sum_{j=1}^{m} a_j \zeta^j + \left(\frac{1}{2} + \sum_{j=1}^{m} b_j \zeta^j\right)\ln\left(\frac{1}{\zeta}\right) + \mathrm{error}_1(k), \tag{44}$$

and

$$E = 1 + \sum_{j=1}^{m} c_j \zeta^j + \left(\sum_{j=1}^{m} d_j \zeta^j\right)\ln\left(\frac{1}{\zeta}\right) + \mathrm{error}_2(k), \tag{45}$$

where $\zeta = 1 - k^2$. The polynomial coefficients are obtained via least-square fits. The sizes of the two error terms depend on m. For example, to guarantee errors of less than 10^{-8} we need $m = 4$ [19, p. 170; 20, p. 591], a very common choice. To guarantee errors of less than 10^{-21}, we need $m = 15$, which is still not excessive.

3.2. *Adaptive Quadratures*

Gaussian quadrature is one of the most popular methods for numerical integration because of its high accuracy. However, the standard Gaussian quadrature lacks the nature of progressiveness; i.e., a Gaussian rule cannot be generated by adding new points to another Gaussian rule, and it has to be reconstructed. This is not suitable for adaptive strategy.

In [21], Kronrod shows that an n-point Gaussian rule may be augmented by a further set of $n + 1$ abscissae to yield a rule which integrates exactly a polynomial of degree $3n + 1$ for n even and $3n + 2$ for n odd. In the extended rule, there are extra $n + 1$ weights and abscissae. While the original Gaussian abscissae remain unchanged, their weights must be reset. Patterson [22] extends this technique by considering the augmentation of an n-point formula by p points. There are tables containing the standard abscissae and weights in [21].

In this study, we use a 7- to 15-point Gauss–Kronrod quadrature. We bisect the integration intervals and estimate the error of the numerical integration over each interval by measuring the difference between the 7-point Gauss quadrature and the 15-point Kronrod rule. A globally adaptive strategy is to bisect the interval with the largest error estimate until the error is less than a prescribed tolerance. We used the freely available software package Quadpack [23] which implements this strategy.

Clenshaw–Curtis quadrature [24] is based on the expansion of the integrand as a series of Chebyshev polynomials. The method is naturally adaptive since it adjusts the number of terms to reach a specified level of accuracy. For integrands with weight functions which cause a slow rate of convergence, Piessens and Brander [25] developed a modified Clenshaw–Curtis quadrature through the computation of modified Chebyshev moments. In this study, we are interested in the computation of the integral with the following weight [23],

$$\int_0^1 f(\alpha') \ln(\alpha')\, d\alpha'. \tag{46}$$

This weight function is one of the choices available in Quadpack which contains the software necessary to perform the modified Clenshaw–Curtis quadrature.

3.3. *Application to the Dipole Distribution*

A convenient choice for the surface coordinate is to use the angle subtended at the center of the enclosed region by the axis of symmetry and the vector to a field point on the initial location of the surface. For the studies reported in this paper, the initial surface is a sphere and α is the polar angle measured from the bottom pole. Thus $\alpha = 0$ will mark the bottom pole, while $\alpha = \pi$ will mark its top.

We approximate the closed surface by a set of points along the contour in the (r, z) meridional plane $(r_i, z_i) \equiv (r(\alpha_i), z(\alpha_i))$ for $i = 1, \ldots, N$, where $\alpha_i = i\pi/(N-1)$. Equations (33), (34) are then enforced at these points. This first requires the computation of ϕ_i and ψ_i. Although the integrands in (35), (36) are continuous when $\alpha = \alpha'$, their derivatives are not. So we split the integrals into two parts: one integrated from 0 to α_i, and the other one from α_i to π. Then we apply the adaptive Gauss–Kronrod quadrature to each of the two integrals. Because the Gauss–Kronrod quadrature is a open quadrature, we do not need to evaluate the integrands at the integration limits. In particular, we do not need to worry about the indeterminate form of the integrand when $\alpha = \alpha'$.

To evaluate the integrands, we also need values for the elliptic integrals and derivatives of r and z. The elliptic integrals are determined through the recursion (41)–(43). Depending on the accuracy we require for the integration, we set a tolerance for the recursion for the elliptic integrals. To determine approximations for the derivatives of r and z, we expand them in a truncated Fourier cosine series: The Fourier coefficients can be determined through the fast Fourier transform in $O(N \ln N)$ operations using the values of r and z at the collocation points. We then differentiate the series analytically and use the fast Fourier transform with the modified coefficients to obtain the derivatives at the collocation points. Similarly we can approximate the derivatives of ϕ and ψ which then give us the velocities of the collocation points on the sheet. To obtain values of quantities at points other than the collocation points, we use quintic splines. Because of the symmetries in a closed, axi-symmetric surface, the endpoint conditions for the splines are easily specified. We call this procedure Method I.

In Method II, we replace the elliptic integral of the first and second kind by the approximations (44), (45). The two integrals (35), (36) then take the form

$$\int_0^\pi f(\alpha,\alpha')\,d\alpha' + \int_0^\alpha g_1(\alpha,\alpha')\ln(\alpha-\alpha')\,d\alpha' + \int_\alpha^\pi g_2(\alpha,\alpha')\ln(\alpha-\alpha')\,d\alpha', \quad (47)$$

where f, g_1, and g_2 are smooth functions of α and α'. We use the Gauss–Kronrod quadrature on the first integral in (47), and the modified Clenshaw-Curtis quadrature on the second and third integrals in (47), respectively. As in Method I, derivatives are obtained through the use of a Fourier cosine series, and interpolation is conducted with quintic splines.

Once the velocity components have been determined by Method I or II, we advance the location of the vortex sheet by applying a fourth-order Adams–Moulton predictor–corrector on (33), (34). Starting values for the predictor–corrector are computed by a standard fourth-order Runge–Kutta method.

4. NUMERICAL TESTS OF METHODS

Our first series of tests are performed without using adaptive quadrature. This provides us with data by which we can compare the effectiveness of adaptive quadrature. What we do explore in these tests is whether different forms for the integrals lead to better numerical evaluation. At issue is the treatment of the singular nature of the integrands.

In Method A, we apply the six-point Gaussian quadrature in each subinterval (α_i, α_{i+1}) of the Biot–Savart integrals (26), (27). This may be viewed as a reasonably accurate method applied in a straightforward way without consideration of the singular nature of the integrand. In Method B, we use the point vortex method, as implemented in [10] with the axi-symmetric Van der Vooren correction. This method results from expressing the integrand as a singular part, treated analytically, and a remainder, treated numerically by the midpoint rule. In Method C, we apply the six-point Gaussian quadrature in each subinterval (α_i, α_{i+1}) of the integrals (35, 36). In all three cases, we use a Fourier series to determine derivatives, and interpolation is performed through the use of quintic splines. The two elliptic integrals are computed through the recursive formulae (41)–(43).

We use the instantaneous velocity field of a uniform flow past a sphere as a test calculation. The parameterization of the surface of the sphere and the dipole distribution is

$$r(\alpha) = \sin(\alpha) \qquad z(\alpha) = -\cos(\alpha) \qquad \mu(\alpha) = \cos(\alpha), \quad (48)$$

where $\alpha \in [0, \pi]$. The velocities of the vortex sheet are

$$r_t = \frac{\sin(2\alpha)}{4} \qquad z_t = -\left(\frac{5}{12} + \frac{1}{4}\cos(2\alpha)\right). \quad (49)$$

We measure the error as the magnitude of the difference between the exact velocity (49) and the numerically calculated one. In Fig. 1, we plot the errors as functions of α for the three different methods when $N = 65$. Even though Method A uses a much higher order quadrature, its errors are about a factor 100 worse than Method B. Clearly, the effort to capture the singular nature of the integrand has paid off. The next step then would be

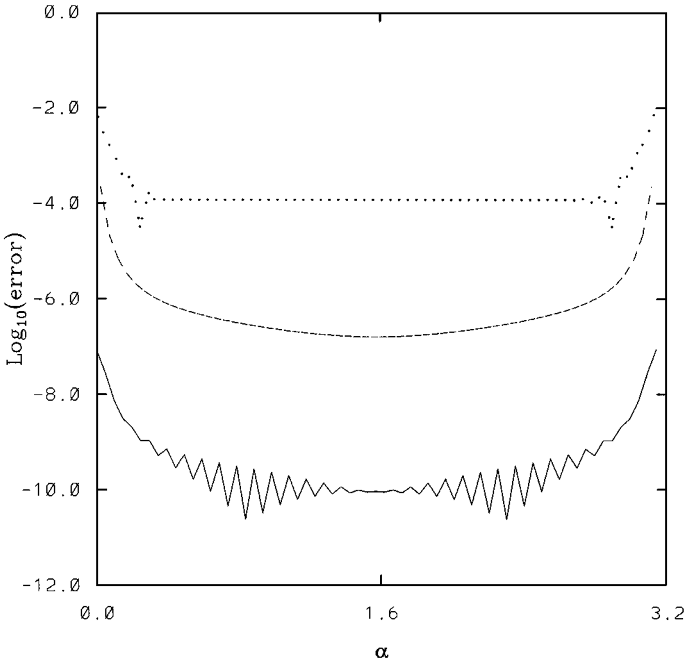

FIG. 1. Errors as functions of α for three non-adaptive methods. Dotted curve: Method A; dashed curve: Method B; solid curve: Method C.

to improve the accuracy of the integration by using a high order Gaussian quadrature. Unfortunately, the cancellation function used to remove the singularity in the integrand is quite complicated and certainly increases the cost of the numerical integration. On the other hand, reducing the singularity in the integrals of the dipole distribution as in Method C is very easy and incurs negligible cost. Method C gives much better results than Method B. In summary, it is important to treat the singular nature of the integrands as explicitly as possible if high order numerical quadrature is to be used to gain high accuracy, and the dipole distribution offers a substantial advantage in that regard.

All three methods lose accuracy when α is near either pole. The cause of the difficulty is the particular behavior of the integrand for a field point near the axis of symmetry [1, 11]. The error profile has a boundary layer inside of which the error only decreases linearly with the spacing between the collocation points [14]. We confirm this behavior in Fig. 2, which shows the variation of the maximum error (which occurs at or near the poles) with the number of collocation points. The decrease is only linear. By linear extrapolation, the error will be about 10^{-7} and 10^{-10} with $N = 2^{20}$ for Methods B and C, respectively. The cost is prohibitive to achieve the levels of accuracy required to study singularity formation on vortex sheets.

There is an interesting feature of the error in Method C, namely, the appearance of a sawtooth pattern. The error profiles in the potential ϕ and the streamfunction ψ are smooth except at the poles, where the integrands are free of any singularities and Gaussian quadrature produces errors that are substantially reduced. The jump in error at the poles has an important consequence on the error in the velocities, which are obtained through differentiation of ϕ and ψ. Since numerical differentiation through a truncated Fourier series of the exact ϕ and ψ produces the exact result, the error in the velocities is just the derivative of the errors

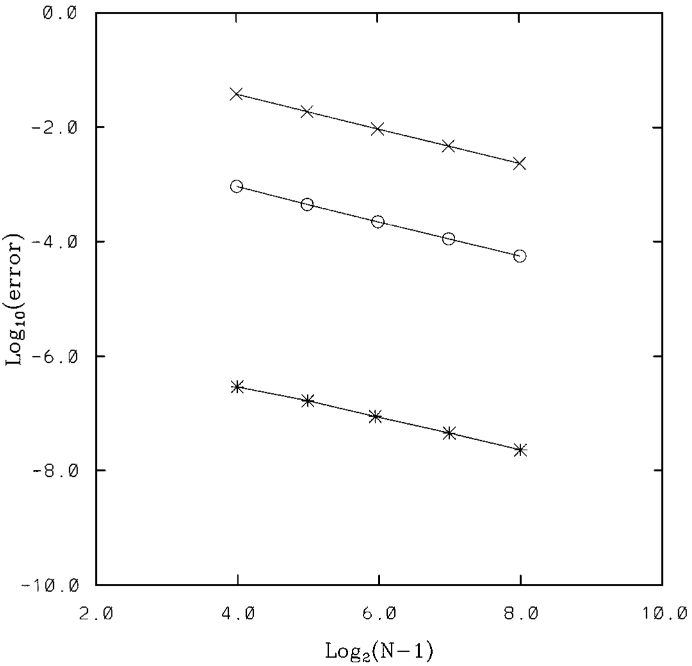

FIG. 2. Log-log plot of the maximum error of each method as a function of N. (x) Method A; (o) Method B; ($*$) Method C.

in ϕ and ψ. Using numerical differentiation through a truncated Fourier series on a jump discontinuity will produce the type of oscillations seen in Method C. Although the errors are quite small, the presence of oscillations may lead to instabilities in a time-dependent calculation.

At this point, the obvious way forward is to use adaptive quadrature, hence Methods I and II. We apply Methods I and II to the same test case as above. For the results reported here, we make sure that the errors in the computation of the elliptic integrals are less than $\epsilon_E = 10^{-14}$. For the adaptive Gauss–Kronrod quadrature (Method A), we use the recursive formulae (41)–(43) until the difference in the iterates is less than ϵ_E. For the adaptive Clenshaw–Curtis quadrature (Method B), we find that $m = 8$ ensures the polynomial approximations to the elliptic functions are accurate to at least ϵ_E. Also, we set a tolerance requirement ϵ_I for the calculation of the various integrals. This tolerance is simply passed through a subroutine call to the software package Quadpack. Figure 3 presents the errors of the two adaptive methods as a function of α when $N = 65$ and $\epsilon_I = 10^{-12}$. In contrast to the non-adaptive methods, the errors are nearly uniform for all α. The errors are very close to the specified tolerance for the calculation of the integrals. Don't forget that ϕ and ψ must be differentiated numerically to determine the velocities on the vortex sheet, and there will be some error incurred as a result.

In order to compare the cost between these two methods, we count the number of integrand evaluations for each method, which is the dominant cost in computing the integrals. In Fig. 4, we plot the average number of integrand evaluations per collocation point as a function of the error. We show the results for both $N = 65$ and $N = 129$. There are several points that these results illustrate. First, consistent with the results of the previous test, it requires many quadrature points to obtain even moderate accuracy. By using an adaptive

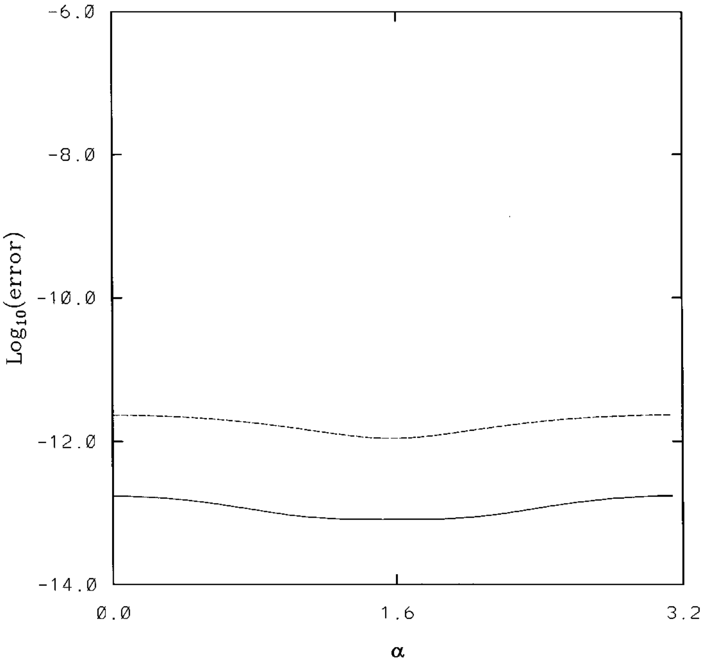

FIG. 3. Errors as functions of α for the two adaptive methods. Solid curve: Method I; dashed curve: Method II.

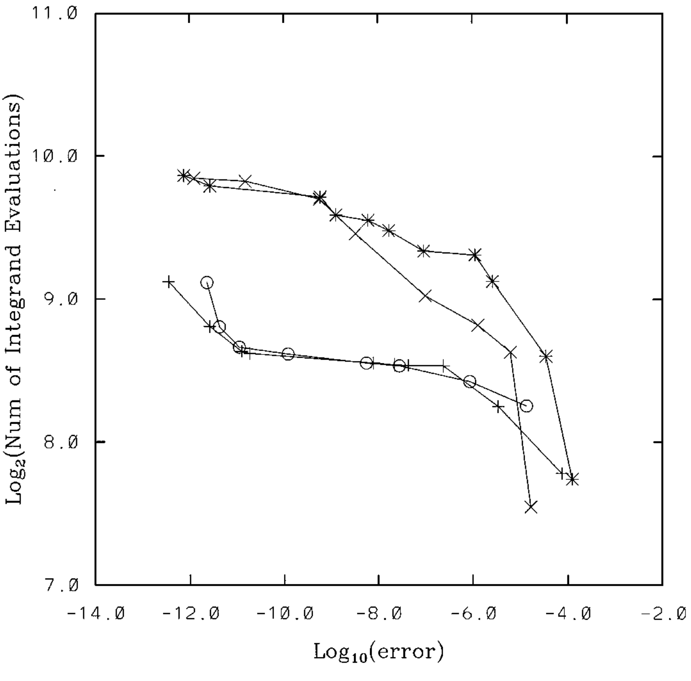

FIG. 4. Log-log plot of the average number of integrands evaluation per collocation point as functions of the errors. (x) Method I with $N = 65$; ($*$) Method I with $N = 129$; (o) Method II with $N = 65$; ($+$) Method II with $N = 129$.

quadrature we insert the quadrature points through interpolation just where they are needed. Without adaption, we would have to introduce many more collocation points, driving up the cost of numerical integration exorbitantly. Note furthermore that the number of integrand evaluations is relatively insensitive to the number of collocation points. This means that the errors in using $N = 65$ and $N = 129$ points to represent the interface are much smaller than the errors caused by the numerical integration. In other words, there is no need to have more collocation points. Finally, we note that Method II is more efficient than Method I. It was unclear to us prior to our testing which method would be more efficient. It seems that the use of a special quadrature to treat the logarithmic part of the integrand is well worth the effort in separating the integrand into two parts. Once again, explicit treatment of singularities and derivative singularities in the integrand pays off.

5. EVOLUTION OF THE VORTEX SHEET

We follow previous work [13, 14] in using (48) as the initial condition. This initial condition corresponds to a uniform potential flow past a solid sphere which is instantaneously dissolved at $t = 0$. The vortex sheet at the boundary of the sphere is then allowed toevolve freely.

Since vortex sheet motion is ill-posed, it is necessary to control the growth of round-off errors to avoid rapid contamination of the profile long before singularity formation. In studies of two-dimensional motion of vortex sheets, a Fourier filter is frequently used [26]: the reliability of the filter has been checked with arbitrary precision calculations [27]. At each time step, we calculate the Fourier spectrum of the location of the vortex sheet and set all amplitudes below a filter level ϵ_F to zero.

In Fig. 5, the profiles of the axi-symmetric vortex sheet are shown at four different times with the last time very close to the time of formation of a curvature singularity. The results are obtained by Method II using $\epsilon_F = \epsilon_I = 10^{-12}$, $N = 257$, and the time step $\Delta t = 0.001$. We establish the accuracy in our results by a resolution study. First, we consider the influence of the number of collocation points N which represent the interface. We treat $N = 257$ as “exact” and use the maximal difference in the sheet location between this “exact” solution and other smaller N as an estimate of the error. We plot the error for $N = 9$, 17, 33, 65, 129 in Fig. 6. Here, the time step is $\Delta t = 0.001$. There are three major sources of error due to the spatial discretization: there is an $O(N^{-6})$ error caused by the use of quintic splines for interpolation; there is an $O(\exp(-cN))$ error in determining the derivatives of ϕ and ψ by their Fourier series (c is some constant); and there is an error produced by the evaluation of the integrals. In general, if the errors in evaluating the integrals are small enough compared with the other two errors, the dominant error should be $O(N^{-6})$. Specifically, the error should decrease by a factor of 64 whenever N is doubled. This is evident in Fig. 6. The errors uniformly decrease by a factor close to 64 as the number of collocation points is increased from $N = 9$ to $N = 65$. For $N = 65$ and $N = 129$, the errors are initially limited by the choices $\epsilon_I = \epsilon_F = 10^{-12}$, but as the errors become larger than 10^{-12}, the accuracy for $N = 129$ is better than for $N = 65$. Despite appearances, the curves are not crossing, but merely touch one another.

Next we consider the errors caused by the temporal discretization. Similar to the spatial resolution study, we take the results for $\Delta t = 0.00025$ as “exact” and use the maximal difference in the sheet location with the results for larger Δt as estimates of the errors. Here, we pick $N = 129$. Since the Adams–Moulton predictor–corrector method has an error of

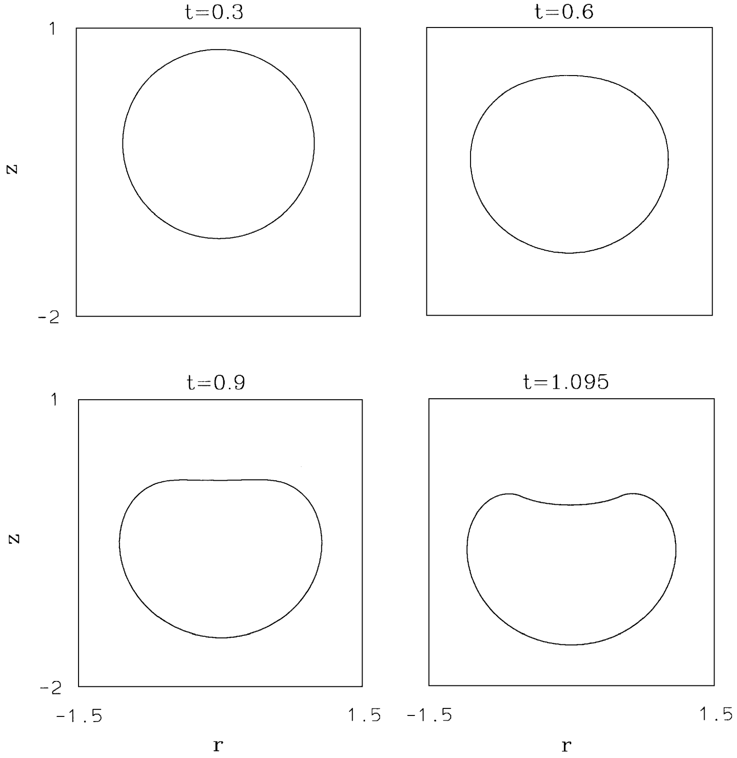

FIG. 5. Profiles of the vortex sheet at different times.

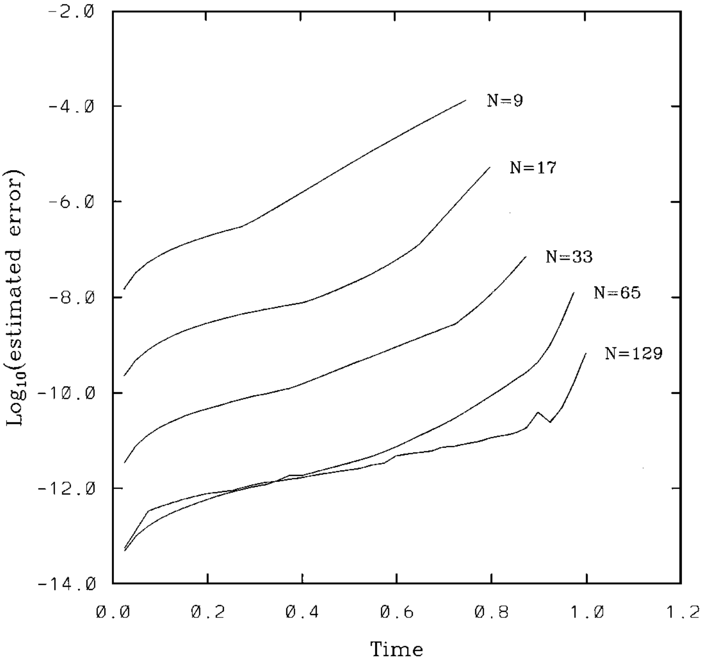

FIG. 6. The maximal magnitude of the difference between the solution for $N = 257$ and smaller N as functions of time.

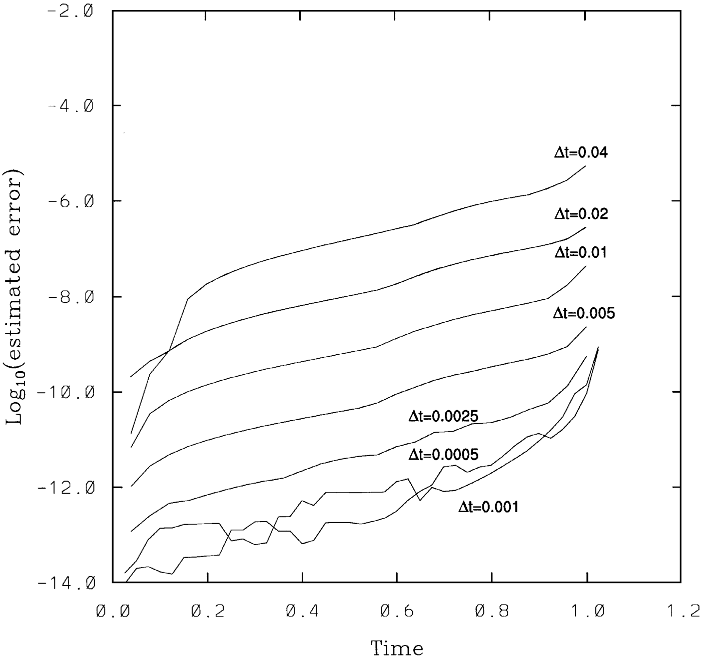

FIG. 7. The maximal magnitude of the difference between the solution for $\Delta t = 0.00025$ and for larger Δt as functions of time.

$O((\Delta t)^4)$, we should obtain an improvement in accuracy of a factor of 16 whenever Δt is halved. In Fig. 7, the errors are plotted as functions of time for various Δt.

Except at very early times, the errors decrease uniformly with a factor of about 16 as Δt decreases to 0.0025. The apparent crossing of the curves for $\Delta t = 0.04$ and $\Delta t = 0.02$ is illusory: the curves merely touch. For smaller values of Δt, the errors become smaller than the effects of the spectral filter ($\epsilon_F = 10^{-12}$), and no further improvement is possible without changing the various tolerance requirements and the filter level. Consequently, $\Delta t = 0.001$ gives the best accuracy for our choice of numerical parameters. Most important is the fact that no smoothing other than the spectral filter to control round-off errors is needed for numerical stability. Highly accurate evaluations of the integrals give numerically stable methods, an observation noted in two-dimensional motion [28, 29].

We turn now to a comparison of the performances of Method I and Method II. From the resolution study, we find that $N = 129$ and $\Delta t = 0.001$ gives levels of accuracy close to $\epsilon_I = 10^{-12}$, so we choose this N and Δt for the comparison of Method I and Method II. We compute solutions for both methods with three different choices of $\epsilon_I = 10^{-8}$, 10^{-10}, 10^{-12} ($\epsilon_I = \epsilon_F$). In Fig. 8, we show the maximal difference in the sheet location of the two solutions. As seen in the plot, the differences are comparable with the size of ϵ_I at early times and increase slightly as time advances. The general tendency of the curves is similar to those shown in the resolution study for Method II. We conclude that the two methods are comparable in terms of achieving accuracy. However, Method II is superior in terms of efficiency. This is evident in Table 1, where the computing time for both methods is listed for different ϵ_I. Roughly speaking, Method II is about four times faster than Method I. The average number of function evaluations per collocation point rises by about a factor of five for both methods, with Method II remaining about a factor of four less throughout

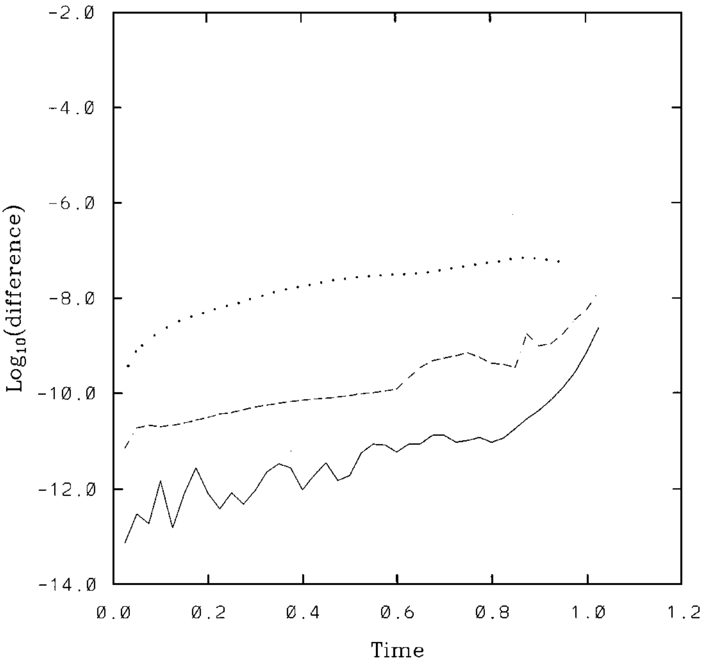

FIG. 8. The maximal magnitude of the difference between the solutions computed by Method I and Method II with different choices of ϵ_I: dotted curve: $\epsilon_a = 10^{-8}$; dashed curve: $\epsilon_a = 10^{-10}$; solid curve: $\epsilon_a = 10^{-12}$.

the evolution. Even so, both methods are very effective considering the accuracy they achieve.

We conclude this section by providing some evidence of the formation of a curvature singularity in the vortex sheet. In Fig. 9 we show profiles of the mean curvature

$$\frac{r_\alpha z_{\alpha\alpha} - z_\alpha r_{\alpha\alpha}}{s_\alpha^{3/2}} + \frac{z_\alpha}{r s_\alpha} \tag{50}$$

at times close to the formation of a curvature singularity. Note that the curvature changes rapidly near where the singularity forms, jumping between a high spike and a low dip. This jump grows in magnitude as the singularity forms even though the location of the sheet (see Fig. 5) shows little evidence of the singularity. This behavior is quite typical of that seen in singularity formation in two dimensional motion of vortex sheets [7]. It is also the reason that the solutions gradually lose their accuracy as time approaches the singularity time, as illustrated in Fig. 7. Depending on the number of collocation points, there is a limit to how close to the singularity time the calculation can approach before the code terminates. The appearance of oscillations in the curvature at $t = 1.08$ and 1.095 is also indicative of insufficient collocation points to resolve the curvature adequately at these times.

TABLE 1
Running Time on SGI Indigo2 Impact 10000

ϵ_I:	10^{-8}	10^{-10}	10^{-12}
Method I (min):	73	115	160
Method II (min):	19	26	35

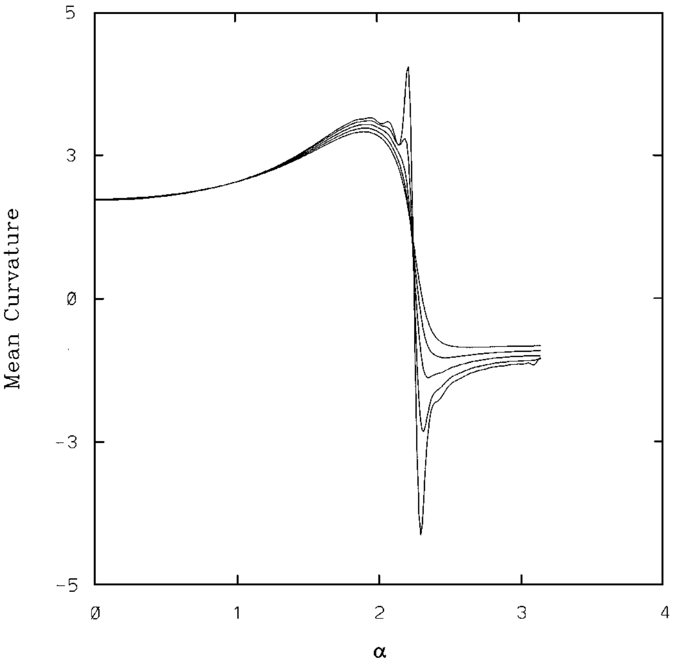

FIG. 9. Profiles of the mean curvature at $t = 1 + i \times 0.02$ ($i = 1, 4$) and $t = 1.095$.

The standard approach used to study the details of singularity formation in two-dimensional vortex sheets is based on fitting the Fourier spectrum of the sheet location to a special form. If branch point singularities are present in the complex α-plane of form

$$r(\alpha) \approx ae^{i\phi}(\alpha - \theta + i\delta)^{\nu+i\lambda} + ae^{-i\phi}(\alpha + \theta + i\delta)^{\nu-i\lambda}, \tag{51}$$

then the Fourier coefficients of r, $\hat{r}_k$ say, take the form

$$\hat{r}_k \approx \frac{a}{k^{\nu+1}} \exp(\sin(k\theta + \lambda \ln k + \phi) \tag{52}$$

for $k \gg 0$. While this is not the place to provide a detailed derivation or justification for these theoretical results, a few words of explanation are in order. The two singularities are placed symmetrical about $\alpha = 0$ with the appropriate form to ensure that r is an even function when α is real. Because the singularities in (51) are below the real axis of α, they affect only the positive part ($k > 0$) of the Fourier spectrum. There will be another pair of singularities above the real axis to ensure that r is real on the real axis, and this pair will affect the negative part of the spectrum. The parameters a, ϕ, θ, δ, ν, and λ can be functions of time. In particular, if δ vanishes in time then the singularities reach the real axis and become physically relevant. The objective of a form-fit to the spectrum then is to identify the presence of such singularities in the complex plane and to verify that they approach the real axis. More details are available in [8, 30] for the two-dimensional case.

Since (52) is an asymptotic form, the commonly accepted procedure [7, 8, 13, 30] for fitting the numerically calculated spectrum is to take six sequential Fourier coefficients and determine local values for the parameters in (52). The next six Fourier coefficient are then used to get new values of the parameters, and the parameters are then plotted as

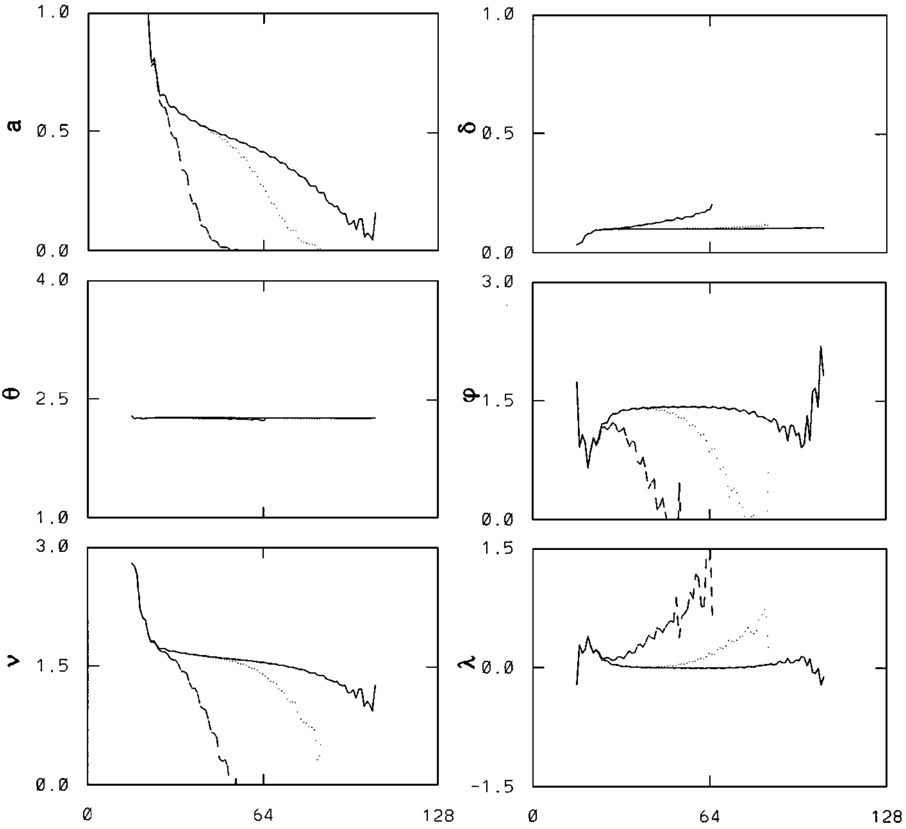

FIG. 10. Parameters in the form-fit of the Fourier spectrum at $t = 1.025$: dashed curve: $\epsilon_f = 10^{-12}$; dotted curve: $\epsilon_f = 10^{-16}$; solid curve: $\epsilon_f = 10^{-20}$.

functions of the local k values. As k increases, the parameters in (52) should settle to constant values.

We show the results of the form-fit in Fig. 10 for three different levels of ϵ_I at time $t = 1.025$. To obtain the results with $\epsilon_I = \epsilon_F = 10^{-16}$, 10^{-20}, we were forced to use quadruple (128 bits) precision. Further, even interpolation with quintic splines proved too inaccurate, so we switched to using a truncated Fourier series for interpolation, thus removing the source of the $O(h^6)$ errors in the numerical integrations. The additional cost for spectral interpolation is small compared to the cost of the numerical integration and is also partly offset by a reduced number of function evaluations per collocation point.

The pattern in the results may be understood as follows. Decreasing ϵ_I improves accuracy, while decreasing ϵ_F allows us to see much more of the Fourier spectrum. For $\epsilon_I = 10^{-12}$, the curves of the parameters in the form-fit do not approach constants except for θ and perhaps δ, the two parameters that determine the location of the singularity in the α-complex plane. To determine the power of the singularity, it is necessary to use much smaller values of ϵ_I. The parameters ν and λ show a clear approach to values consistent with the theoretical prediction $\nu = 1.5$ and $\lambda = 0$ when $\epsilon_I = 10^{-20}$. We would not be able to confirm theoretical predictions if we did not use such a small value of ϵ_I. Note that for larger values of k, the form-fits deteriorate because of truncation errors in the spectrum and the influence of the filter. This contamination is delayed for the smaller values of ϵ_I and ϵ_F.

Now that we have adequate accuracy to study the presence of singularities in the α-complex plane, we can study the nature of their origin and how they approach the real axis. Details will be presented in [31].

6. CONCLUSIONS

Many quadrature points are needed to evaluate boundary integrals accurately for the axi-symmetric motion of a vortex sheet. If a fixed quadrature rule is used, this also requires many collocation points, driving the cost to prohibitive levels. By using adaptive quadratures, the number of quadrature points can be made independent of the number of collocation points, leading to more efficient techniques for the numerical study of vortex sheet motion. In particular, we can ensure sufficient accuracy to locate and confirm the nature of singularities in the α-complex plane. These singularities, when they reach the real α axis, are the cause of curvature singularities in the vortex sheet.

We anticipate similar results for boundary integral methods to track free surface motion in axi-symmetric geometry.

ACKNOWLEDGMENTS

We thank Professor D. W. Moore for many valuable discussions and providing us with his code for Method B. We also benefited from several conversations with Monika Nitsche. Some of the computations were performed at the Ohio Supercomputer Center, whose grant of computing resources is gratefully acknowledged. Other computations were done at the University of Minnesota Supercomputing Institute through a grant for the Mathematics in High Performance Computing Year (1997) held at the Institute for Mathematics and Its Applications.

REFERENCES

1. G. R. Baker, D. I. Meiron, and S. A. Orszag, Generalized vortex methods for free-surface flow problems. *J. Fluid Mech.* **123**, 477 (1982).
2. C. Pozrikidis, *Boundary Integral and Singularity Methods for Linearized Viscous Flow* (Cambridge Univ. Press, Cambridge, UK, 1992).
3. G. R. Baker and D. W. Moore, The rise and distortion of a two-dimensional gas bubble in an inviscid liquid, *Phys. Fluids A* **1**, 1451 (1989).
4. G. R. Baker, D. I. Meiron, and S. A. Orszag, Vortex simulations of the Rayleigh–Taylor instability, *Phys. Fluids* **23**, 1485 (1980).
5. G. R. Baker, Generalized vortex methods for free-surface flows, in *Waves on Fluid Interfaces*, edited by R. E. Meyer (Academic Press, New York, 1983).
6. A. Sidi and M. Israeli, Quadrature methods for periodic singular and weakly singular Fredholm integral equations, *J. Sci. Comput.* **3**, 201 (1988).
7. M. J. Shelley, A study of singularity formation in vortex sheet motion: A spectrally accurate method, *J. Fluid Mech.* (1992).
8. G. R. Baker, R. E. Caflisch, and M. Siegel, Singularity formation during Rayleigh–Taylor instability, *J. Fluid Mech.* (1993).
9. G. R. Baker, D. I. Meiron, and S. A. Orszag, Boundary integral methods for axisymmetric and three-dimensional Rayleigh–Taylor instability problems, *Physica D* **12**, 19 (1984).
10. B. Bernadinis and D. W. Moore, A ring-vortex representation of an axisymmetric vortex sheet, in *Studies of Vortex Dominated Flows* (Springer-Verlag, Berlin/New York, 1987), p. 33.
11. M. Nitsche, Axi-symmetric vortex sheet motion: Accurate evaluation of the principal value integral, preprint, 1997.

12. T. S. Lundgren and N. N. Mansour, Oscillations of drops in zero gravity with weak viscous effects, *J. Fluid Mech.* (1988).
13. D. A. Pugh, *Development of Vortex Sheets in Boussinesq Flows—Formation of Singularities*, Ph.D. thesis, Imperial College of Science and Technology, 1989.
14. M. Nitsche, Evolution of a cylindrical and spherical vortex sheet, in *Proceedings of Second International Workshop on Vortex Flows and Related Numerical Methods*, 1995.
15. R. E. Caflisch and Xiao-Fan Li, Lagrangian theory for 3D vortex sheets with axial or helical symmetry, *Transport Theory Statist. Phys.* **21**, 559 (1992).
16. M. Jaswon and G. Symm, *Integral Equation Methods in Potential Theory and Elastostatics* (Academic Press, New York, 1977).
17. G. Batchelor, *An Introduction to Fluid Dynamics* (Cambridge Univ. Press, Cambridge, UK, 1967).
18. P. F. Byrd and M. D. Friedman, *Handbook of Elliptic Integrals for Engineers and Physicists* (Springer-Verlag, Berlin/New York, 1953).
19. C. Hastings, Jr., *Approximations for Digital Computers* (Princeton Univ. Press, Princeton, NJ, 1955).
20. M. Abramowitz and I. A. Stegun, *Handbook of Mathematical Functions* (Dover, New York, 1970).
21. A. S. Kronrod, *Nodes and Weights of Quadrature Formulas* (Consultants Bureau, New York, 1965).
22. T. N. Patterson, The optimum addition of points to quadrature formulae, *Math. Comp.* **22**, 847 (1968).
23. R. Piessens, E. de Doncker-Kapenga, C. W. Uberhuber, and D. K. Kahaner, *Quadpack* (Springer-Verlag, Berlin/New York, 1983).
24. C. Clenshaw and A. R. Curtis, A method for numerical integration on an automatic computer, *Numer. Math.* **12**, 197 (1960).
25. R. Piessens and M. Branders, The evaluation and application of some modified moments, *BIT* **13**, 443 (1973).
26. R. Krasny, A study of singularity formation in a vortex sheet by the point vortex approximation, *J. Fluid Mech.* **167**, 65 (1986).
27. J. Ely and G. R. Baker, High precision calculations of vortex sheet motion, *J. Comput. Phys.* **111**, 275 (1994).
28. A. J. Roberts, A stable and accurate numerical method to calculate the motion of a sharp interface between fluids, *IMA J. Appl. Math.* **31**, 13 (1983).
29. A. Nachbin and G. R. Baker, Stable methods for vortex sheet motion in the presence of surface tension, *SIAM J. Sci. Comput.* (to appear).
30. S. J. Cowley, G. R. Baker, and S. Tanveer, On the formation of Moore curvature singularities in vortex sheets, *J. Fluid Mech.* (to appear).
31. G. R. Baker and Q. Nie, Singularity formation in an axi-symmetric vortex sheet, in preparation.